ADVANCING EARTH AND SPACE SCIENCES

JGR Solid Earth

RESEARCH ARTICLE
10.1029/2024JB030465

Laboratory Measurement of Sonic (1–20 kHz) P-Wave Velocity and Attenuation During Melting of Ice-Bearing Sand

Hanif S. Sutiyoso[1,2], **Sourav K. Sahoo**[2], **Laurence J. North**[2], **Ismael Himar Falcon-Suarez**[2], **Timothy A. Minshull**[1], and **Angus I. Best**[2]

[1]School of Ocean and Earth Science, University of Southampton, Southampton, UK, [2]National Oceanography Centre Southampton, Southampton, UK

Key Points:

- We present measurements of elastic wave properties at sonic frequencies in ice-bearing sand during melting
- Ice melting decreases velocity and increases attenuation, with the largest changes occurring at higher ice saturations
- Velocity is sensitive to changes in ice content across all frequencies, while attenuation is most sensitive at higher frequencies

Supporting Information:

Supporting Information may be found in the online version of this article.

Correspondence to:

H. S. Sutiyoso,
hss1g15@soton.ac.uk

Citation:

Sutiyoso, H. S., Sahoo, S. K., North, L. J., Falcon-Suarez, I. H., Minshull, T. A., & Best, A. I. (2025). Laboratory measurement of sonic (1–20 kHz) P-wave velocity and attenuation during melting of ice-bearing sand. *Journal of Geophysical Research: Solid Earth*, *130*, e2024JB030465. https://doi.org/10.1029/2024JB030465

Received 3 OCT 2024
Accepted 31 MAR 2025

Author Contributions:

Conceptualization: Hanif S. Sutiyoso, Sourav K. Sahoo, Angus I. Best
Data curation: Hanif S. Sutiyoso
Formal analysis: Hanif S. Sutiyoso
Funding acquisition: Sourav K. Sahoo
Investigation: Hanif S. Sutiyoso
Methodology: Sourav K. Sahoo, Laurence J. North
Project administration: Sourav K. Sahoo, Timothy A. Minshull, Angus I. Best
Resources: Sourav K. Sahoo, Laurence J. North, Timothy A. Minshull, Angus I. Best
Software: Laurence J. North

Abstract

We measured the acoustic properties of ice-bearing sand packs in the laboratory using an acoustic pulse tube within the frequency range of 1–20 kHz, similar to sonic well-logs. We analyzed how wave velocity and attenuation (the inverse of quality factor) change with ice saturation and measurement frequency during melting. We found strong frequency-dependent correlations for both acoustic parameters with ice saturation. For any frequency within the studied range, velocity decreases and attenuation increases as the ice melts. For lower ice saturations ($S_i < \sim 0.5$), attenuation was particularly sensitive to frequency linked to acoustic wave scattering from patchy ice saturation. We used rock physics models with three-phase approaches to assess our experimental results. The comparison highlights the influence of ice formation distribution (i.e., uniform vs. patchy), permeability, and gas content on both velocity and attenuation. Our results pave the way for monitoring ice saturation from sonic measurements, as ice saturation has contrasting effects on velocity and attenuation, and the effects vary with frequency. Overall, this research contributes to a better understanding of the acoustic response of ice-bearing sediments and provides valuable insights for various applications, including permafrost monitoring and natural gas hydrate dissociation studies.

Plain Language Summary

Understanding how sound moves through frozen ground is important for studying changes in the Earth's surface, such as melting permafrost. Our study looks at how sound waves travel through sand that contains ice and how this changes as the ice melts, similar to what happens when permafrost thaws due to global warming. We ran laboratory experiments to measure how fast sound moves and how much energy is lost as the ice melts, using sound frequencies similar to those used in underground surveys. We found that when ice melts, sound travels more slowly, and more energy is lost. These effects also depend on the frequency of the sound waves. Our findings help to estimate how much ice is in the ground by analyzing sound waves, which is also useful for studying gas hydrates—ice-like matter that traps greenhouse gases underground. This study can improve our ability to monitor permafrost stability and gas hydrate deposits.

1. Introduction

Understanding the elastic properties of ice-bearing sediments is crucial for various geophysical applications, such as understanding climate-induced permafrost degradation (Tourei et al., 2024) and quantifying gas hydrate deposits (e.g., Guerin & Goldberg, 2002; Lin et al., 2018; Ruppel & Kessler, 2017). As permafrost thaws, it can release significant amounts of methane, a potent greenhouse gas primarily stored as gas hydrates (Kvenvolden, 1988), into the atmosphere. This process would exacerbate global warming (e.g., Kvenvolden, 1993; Schuur et al., 2015), and impact infrastructure stability (e.g., Hjort et al., 2022). Thus, relating elastic wave properties to ice or hydrate content is key for monitoring and managing these environmental challenges.

Elastic wave properties, such as velocity and attenuation, can be measured across a broad frequency spectrum depending on the spatial scale required, that is, from seismic surveys and sonic well-logging to ultrasonic laboratory experiments. Frequency controls the degree of velocity dispersion (e.g., Ahmed et al., 2022; Oda et al., 1990; O'Hara, 1985), which is related to attenuation through the causality principle (Kolsky, 1964). Therefore, understanding frequency dependence is essential for comparing acoustic properties at different spatial scales.

Compressional wave velocity and attenuation are both sensitive to pore fluid content (e.g., Barriere et al., 2012; Berryman, 1981; Knight and Nolen-Hoeksema, 1990; Rubino & Holliger, 2012). The relationship between elastic

Supervision: Sourav K. Sahoo, Timothy A. Minshull, Angus I. Best
Validation: Sourav K. Sahoo, Angus I. Best
Visualization: Hanif S. Sutiyoso
Writing – original draft: Hanif S. Sutiyoso
Writing – review & editing: Hanif S. Sutiyoso, Sourav K. Sahoo, Ismael Himar Falcon-Suarez, Timothy A. Minshull, Angus I. Best

wave properties and pore fluid content is often complex in nature, potentially requiring multiple measurement techniques and costly in-situ observations to achieve a thorough understanding. To address this challenge, controlled laboratory experiments offer a viable alternative. However, these studies are commonly performed at ultrasonic frequencies (150 kHz–1 MHz), where properties may differ from those measured in the field using seismic (∼100 Hz) and sonic logging (∼10–25 kHz) methods. Likewise, laboratory studies on ice-bearing rocks have focused on linking geophysical and geomechanical properties at ultrasonic frequencies (e.g., Chang et al., 2021; Matsushima et al., 2008), which are also relevant to gas hydrate-bearing sediments due to the similarity in compressional wave characteristics between hydrate and ice (Best et al., 2013; Helgerud et al., 2009). However, to bridge the gap between ultrasonic laboratory experiments and field seismic surveys of permafrost (e.g., Bustamante et al., 2023; James et al., 2021; Wagner et al., 2019), further studies at sonic frequencies are needed.

Theoretical rock physics models have been influential in studying how pore content affects elastic wave properties, particularly in ice/cryosphere research (e.g., Leclaire et al., 1994; Li & Matsushima, 2024). These models can be either two-phase: sediment and pore fluid, or three-phase: sediment, ice (or hydrate), and pore fluid (e.g., Leclaire et al., 1994; Marín-Moreno et al., 2017). Current models accounting for velocity dispersion are primarily based on Biot's theory (Biot, 1956, 1962) and are applied to unconsolidated sediments and porous rocks. A notable example is Leclaire et al. (1994)'s model, which extends Biot's theory to predict elastic wave parameters in frozen media. This model incorporates ice parameters into Biot's theory, assuming no direct contact between the sediment matrix and ice that is separated by unfrozen water, except in the limited case of a fully frozen medium. Rock physics models developed for gas hydrate studies can also explain ice-bearing sediment cases due to the similarity in gas hydrate and ice properties (Gabitto & Tsouris, 2010; Helgerud et al., 2009; Marín-Moreno et al., 2017; Pearson et al., 1983).

In this study, we present and assess a novel experimental data set of compressional (P-) wave velocity and attenuation of sand packs as a function of ice saturation across the 1–20 kHz frequency range. Our results show that P-wave velocity and its attenuation depend on both saturation and frequency. Using LeClaire's model (Leclaire et al., 1994) and the hydrate-bearing effective sediment (HBES) approach (Marín-Moreno et al., 2017), we analyze our findings to better understand the mechanisms driving our experimental observations and provide new insights for improving ice content estimations from field measurements.

2. Methods

2.1. Sample Preparation and Description

We used clay-free Leighton Buzzard sand with a mean grain diameter of 100 μm in a 0.5 m long polyvinyl chloride (PVC) cylindrical pipe with an outer diameter of 0.069 m (Figure 1a). The acoustic impedance of the PVC material is 2.9×10^6 kg m^{-2} s^{-1}, derived from a velocity of 2,600 m s^{-1} and a density of 1,120 kg m^{-3} (Selfridge, 1985). Meanwhile, the acoustic impedance of the sand pack is 2.2–6.8 $\times 10^6$ kg m^{-2} s^{-1}, derived from velocities of 1,450–3,600 ms^{-1} and densities of 1,460–1,890 kgm^{-3}, covering both water-saturated (lower impedance) and ice-bearing states (higher impedance) (Kang et al., 2021; Schumann et al., 2014). We sealed both ends of the pipe with PVC endcaps to ensure hydrostatic pressure was uniformly applied across the sand pack during the experiment.

We prepared the samples by pouring the sand into the PVC pipe (fitted with the bottom endcap) and tamping it in successive layers for even compaction. To prevent impedance contrasts between layers, we evenly scratched the top part of each layer. Once the sand was fully compacted in the pipe, we saturated the sample by flowing a pre-calculated amount of de-ionized water into the sand pack within the pipe, increasing the sample saturation by ∼10%, stepwise. Before proceeding with the freezing, we measured the acoustic properties of the water-saturated sample in the pulse tube to provide baseline measurements of the acoustic properties at water-saturated or fully-melted conditions.

For this experiment, we prepared two samples (denoted as Samples 1 and 2). We estimated the empirical porosity (ϕ) by wet-dry mass balance, resulting in $\phi_1 = 0.408 \pm 0.01$ and $\phi_2 = 0.413 \pm 0.01$. Then, using the bulk dry density (ρ_b) estimated for each sample ($\rho_{b1} = 1.611 \pm 0.033$ g/cm^3; $\rho_{b2} = 1.613 \pm 0.033$ g/cm^3) and the average density of the solid particles (ρ_s), we contrasted the empirical values with the theoretical porosity (ϕ_T) resulting from $\phi_T = 1 - \rho_b/\rho_s$, which assumes fully saturation. These estimates resulted in ice saturation discrepancies of

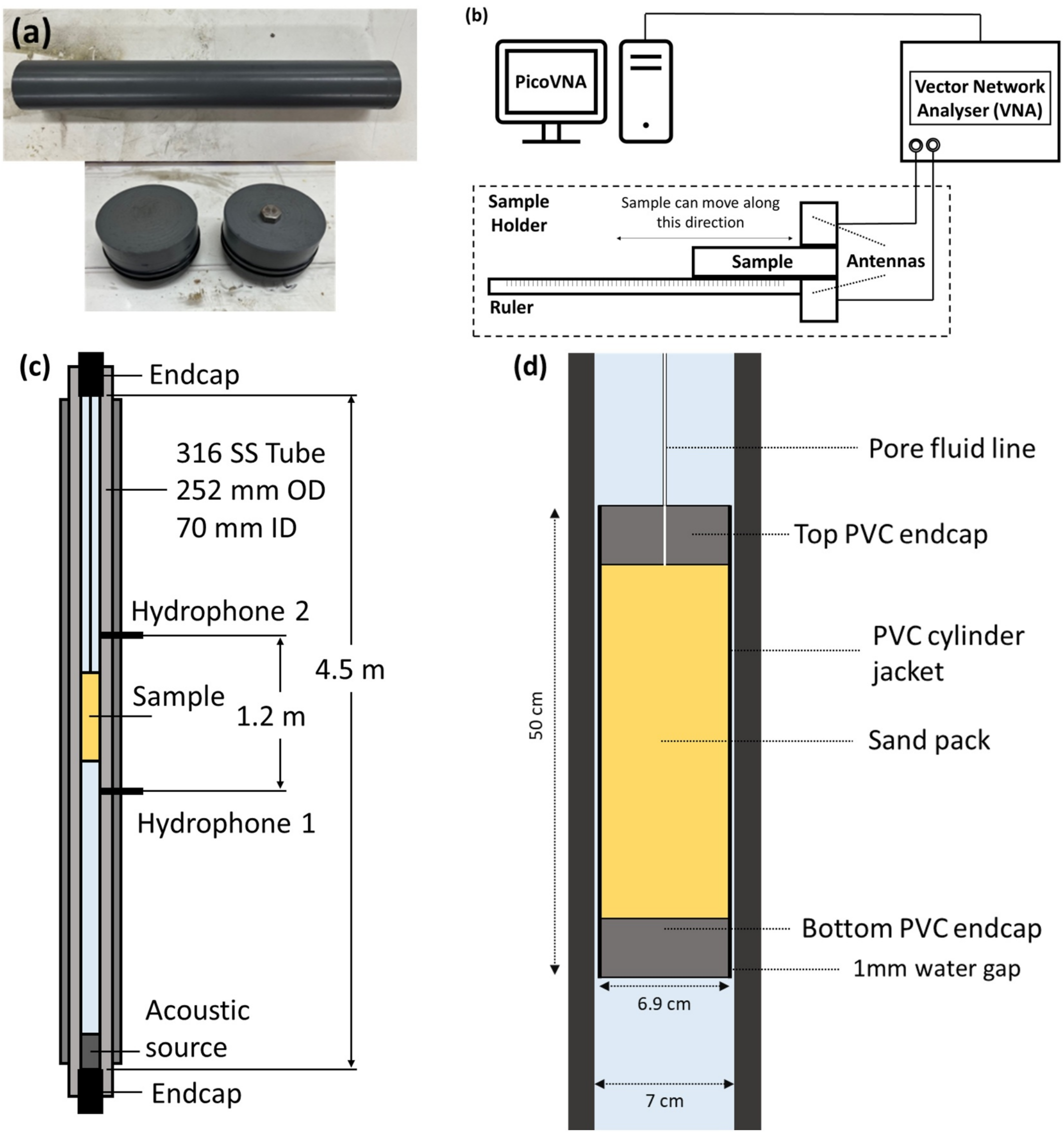

Figure 1. Experimental setup: (a) 50 cm length polyvinyl chloride (PVC) cylinder jacket and PVC endcaps, (b) schematic diagram of the experimental microwave setup, (c) dimensions of the pulse tube and its components, and (d) a zoomed-in view of the PVC-jacketed sample inside the pulse tube.

~6% and ~7% for Samples 1 and 2, respectively, which are the experimental uncertainties associated with the saturation process due to non-connected porosity (e.g., Falcon-Suarez et al., 2024).

For the ice-bearing sand preparation, we froze the samples in a freezer at a controlled temperature of −10°C for 48 hr to ensure maximum conversion of pore fluid to ice. Releasing gas bubbles during sand saturation helped minimize bubble formation during ice formation, ensuring more consistent laboratory measurements (McCutchan & Johnson, 2022). We used a non-destructive microwave measurement technique to image ice distribution and melting within Sample 2 at a controlled room temperature of 19°C (Figure 1b), which leads to ~5.9% error (Sutiyoso, Sahoo, North, et al., 2024). We monitored the ice content by taking microwave readings at 2 cm intervals along the sample length.

2.2. Pulse Tube Measurement

We conducted the experiment using a 4.5-m-long acoustic pulse tube at the National Oceanography Center (NOC) Southampton (Figure 1). The tube uses an acoustic waveguide concept, consisting of a water-filled, thickwalled, stainless steel cylindrical tube as the waveguide to axially propagate plane waves, as also argued by McCann et al. (2014) based on the theory of Dubbelday and Capps (1984). An acoustic piezo-electric transducer located at the bottom insonifies the sample within the 1–20 kHz range using variable frequency chirp signals (see in Supporting Information S1). We performed the measurements at a confining pressure (P_c) of 2.5 MPa, and atmospheric pressure (P_p) (i.e., effective pressure, $P_{\mathrm{eff}} = P_c – P_p \sim 2.5$ MPa) and a controlled temperature of 19°C, for all samples. These experimental conditions aim to simulate the melting of permafrost active layer and gas hydrate dissociation (Dobiński, 2020; Voronov et al., 2016).

The measurements consisted of a time series of signal amplitude in voltage from the sample throughout the ice saturation (Figure 2a). We used a Fast Fourier Transform method to obtain the impulse response by deconvolving the raw signals with the source. Then, we applied time-domain gating to eliminate multiple reflections from the pulse tube endcaps. Lastly, we used an inversion model incorporating the scattering matrix method to determine complex velocity and attenuation for each frequency component. Examples of measured and deconvolved signals are shown in Figure 2, and details of the processing workflow are provided in Sutiyoso, Sahoo, and North (2024).

The pulse tube geometry constrains wave propagation to a quasi-plane (lowest order) wave mode below the cut-off frequency for higher-order modes (Wilson et al., 2003), in this case, approximately 20 kHz. This quasi-plane mode allows the pulse tube to directly measure plane or body wave propagation within the samples. This has been confirmed with finite element modeling (FEM) and measurements of materials with known elastic properties, for example, Nylon 66 (see in Supporting Information S1).

The calibration process involves comparing pulse tube measurements with theoretical transmission coefficients to determine velocity and attenuation errors. The error bounds are defined as the parameter values where the sum of squares of the residuals between experimental and theoretical coefficients reached 10% higher than the best-fit solution (McCann et al., 2014). Our experimental uncertainties are ±2.4% and ±5.8% for velocity and attenuation, respectively. Experimental results agreed with ultrasonic measurements when projected into the sonic range using a standard linear solid model, which accounted for attenuation and velocity dispersion. This analysis confirmed that similar compressional waves propagated through the material in both methods. Additionally, the velocity of the water-filled PVC jacket was compared with both the water-filled pulse tube and the theoretical model by Belogol'skii et al. (1999), also showing strong agreement. This consistency indicates that the same compressional waves travel through the pulse tube. Both calibration procedures are explained in detail by North and Best (2015) and Sutiyoso, Sahoo, and North (2024).

Anomalous results are observed both in calibration measurements and FEM below frequencies corresponding to a ratio of propagating wavelength to sample length of ½. FEM shows this effect only for rigid solids (with a significant shear modulus). We interpret this as the result of the piston-like movement of the sample within the pulse tube, resulting in significant viscous losses in the thin water layer between the sample and the pulse tube walls. The FEM results are provided in Supporting Information S1.

2.3. Ice Saturation Estimates and Modeling

We established a baseline by measuring the velocity and attenuation of the sample fully saturated in water but before freezing (i.e., melted state, $S_i = 0$). Then, we assumed $S_i = 1$ when the sample entered the pulse tube, although keeping in mind that some unfrozen water might still be present, such as thin water films bound to grains (Dash et al., 1995; Watanabe & Mizoguchi, 2002). However, the melting process started before our first measurement due to the time required to reach the target pressure in the pulse tube. Thus, we predicted the velocity and attenuation at full ice saturation using a regression model. The estimated ice saturation is derived from the following empirical relationship:

$$S_i = 1 - \left(\frac{t}{T}\right)^n, \tag{1}$$

where S_i is ice saturation, t is the elapsed measurement time (in seconds), T is the total time for complete melting (determined by velocity and attenuation at the fully melted state), and n is an empirical parameter expressing the exponential relationship between ice melting and time (McCutchan & Johnson, 2022). We estimated n from the best fit of our experimental results to the rock physics models of Leclaire et al. (1994) and Marín-Moreno et al. (2017). Both models incorporate Biot's theory to predict frequency-dependent velocity and attenuation, but

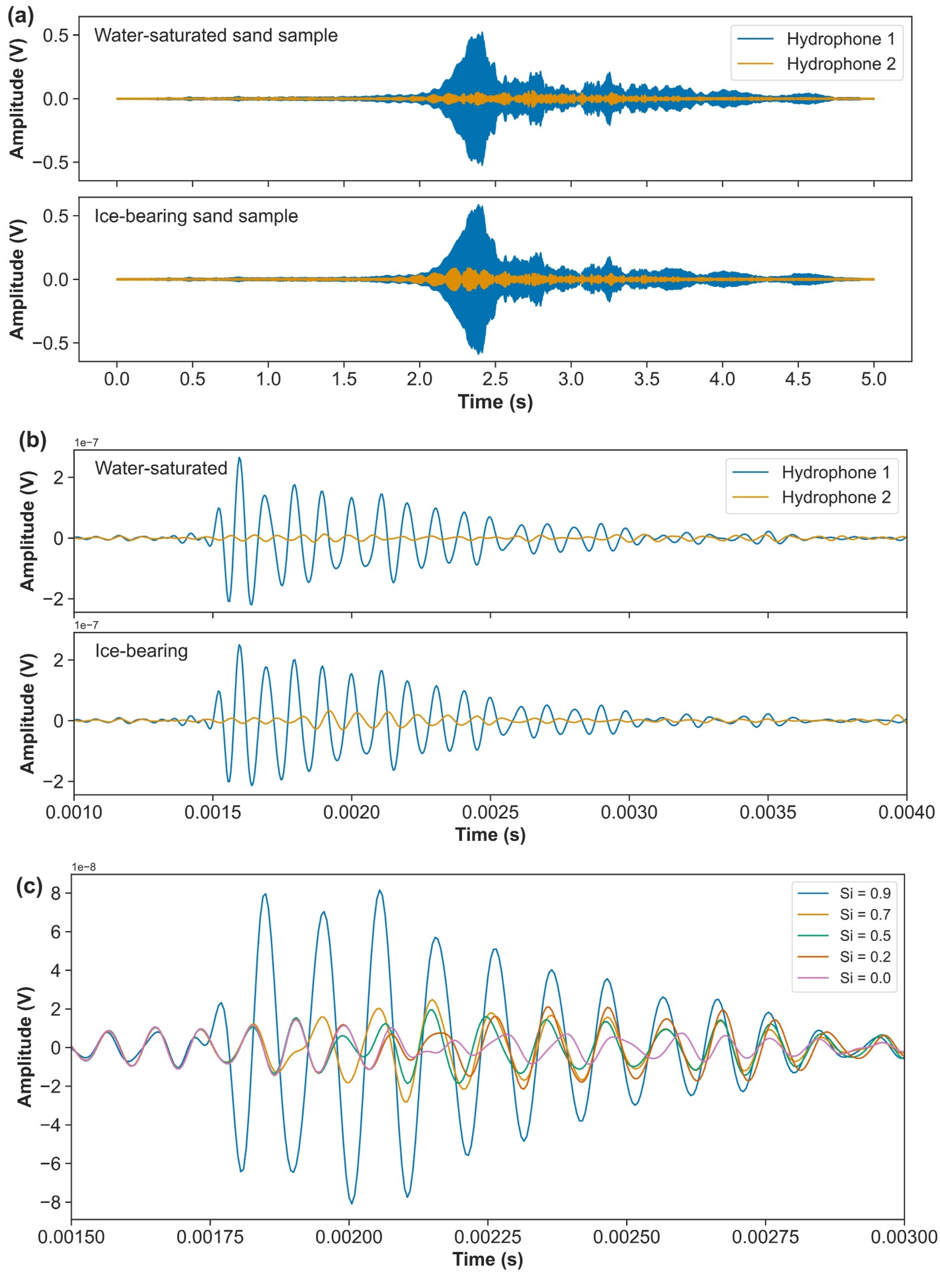

Figure 2. Time series record from pulse tube measurements. (a) An example of recorded time series (raw) signal, (b) Deconvolved signals for the water-saturated (fully melted state) and ice-bearing (fully frozen state) sand samples from the readings of both hydrophones (as displayed in Figure 1c), and (c) Zoomed-in view of deconvolved signals from hydrophone 2 at different ice saturation (S_i).

10.1029/2024JB030465

Table 1
Fixed and Case-Dependent Input Parameters Used in the Model Runs (Case-Dependent Parameters Only Used in Hydrate-Bearing Effective Sediment Model Runs)

Parameter	Value	Units	Reference
Fixed input parameters			
Experimental conditions			
Effective pressure	2.5×10^6	Pa	
Temperature	19	°C	
Sand sediment properties			
Porosity without ice	0.41		Measured
Critical porosity	0.38		
Sand grain bulk modulus	36×10^9	Pa	Simmons (1965)
Sand grain shear modulus	45×10^9	Pa	Simmons (1965)
Sand grain density	2650	kgm^{-3}	Simmons (1965)
Sand grain diameter	1×10^{-4}	m	Best et al. (2013)
Coordination number	9		Murphy (1982)
Tortuosity	3		Berryman (1981)
Ice grain properties			
Ice bulk modulus	5.5×10^9	Pa	Chang et al. (2021)
Ice shear modulus	2.7×10^9	Pa	Chang et al. (2021)
Case-dependent input parameters			
Pore-filling concentration	0.0–1.0		
Sand frame permeability	0.25–10	Darcy	
Gas saturation	0–0.05		
Gas bubble radius	0.01–10	mm	

consider the rock frame differently. Biot's theory (Biot, 1956, 1962) is a widely used model for unconsolidated sediments (e.g., Cadoret et al., 1998; Chotiros, 1995; Williams et al., 2002), which accounts for the frequency dependence of the acoustic attributes due to fluid viscosity and inertial interaction between pore fluid and sediment matrix.

Leclaire et al. (1994) extended Biot's theory to predict elastic wave parameters in frozen media. This model uses a three-phase approach with sediment (matrix), ice, and unfrozen water, which can coexist, incorporating ice parameters into Biot's theory. The model assumes no direct contact between sediment matrix and ice due to thin water film formation around sediment grains, except for the fully frozen media case. Marín-Moreno et al. (2017) proposed the HBES model, which was developed from Best et al.'s (2013) hydrate effective grain model. This model predicts velocity and attenuation dispersion based on the clay-squirt flow mechanism in sediment (Leurer, 1997; Leurer & Brown, 2008) by incorporating the Biot-Stoll fluid flow model (Stoll & Bryan, 1970). It calculates acoustic properties using the complex bulk modulus of both the pore fluid (water, gas, and pore-filling (PF) hydrate) and the solid phases (sediment grains and cementing hydrate). HBES uses the Reuss approximation (Reuss, 1929) to calculate the effective fluid bulk modulus. We extended the model by adding the Voigt and Brie approximations (Brie et al., 1995; Voigt, 1889) to explore the effect of ice distribution on the acoustic properties. We used Brie's coefficient (e) equal to 5, which positioned Brie's approximation between Voigt's and Reuss' (Brie et al., 1995). To apply the HBES model to ice-bearing sediments, we simplified the model by assuming there is no gas and fluid inclusion inside the ice grains, and we replaced the bulk and shear modulus parameters of hydrate grains with those of ice grains (see model inputs in Table 1).

First, we compared both models with the experimental data to determine the best fit. Using the best-fit model, we varied morphology, permeability, gas saturation, and gas bubble size. The initial settings were 100% PF morphology, 1 Darcy permeability, and 0% gas saturation. We adjusted one parameter at a time, keeping the others constant until the objective function (Equation 2) showed minimal improvement, indicating the best fit. The function works well if velocity and attenuation vary by similar factors, which holds true for the current data set. However, if both parameters exhibited significantly different variation magnitudes, one parameter could disproportionately influence the objective function.

$$\text{Objective function} = \frac{|V_{\text{experimental}} - V_{\text{modelled}}|}{V_{\text{experimental}}} + \frac{|Q^{-1}_{\text{experimental}} - Q^{-1}_{\text{modelled}}|}{Q^{-1}_{\text{experimental}}} \quad (2)$$

3. Results

3.1. Inferring Ice Saturation

Figure 3a shows ice melting began from both the top (35–45 cm) and bottom (0–5 cm) sections (e.g., at $S_i = 0.95$), where the melting progressed faster compared to the middle part of the column (e.g., $S_i = 0.76$ and 0.48). The microwave image represents only Sample 2, but we assume the distribution will be similar in both samples due to the similarity in properties. Ice in the middle-to-bottom section (5–15 cm) melted more slowly, especially as saturation dropped to $S_i = 0.28$, before stabilizing at low ice saturation levels (e.g., $S_i = 0.06$). The ice saturation averaged over the sample against melting time (Figure 3b), shows an exponential decay in ice saturation over time (a steep initial drop that slows around 180 min). We compared these measurements with an ice melting model (Equation 1) using different n values, representing an empirical parameter. Most data points fit well within the curves for $n = 1.0–1.4$, suggesting this range best captures the observed melting behavior.

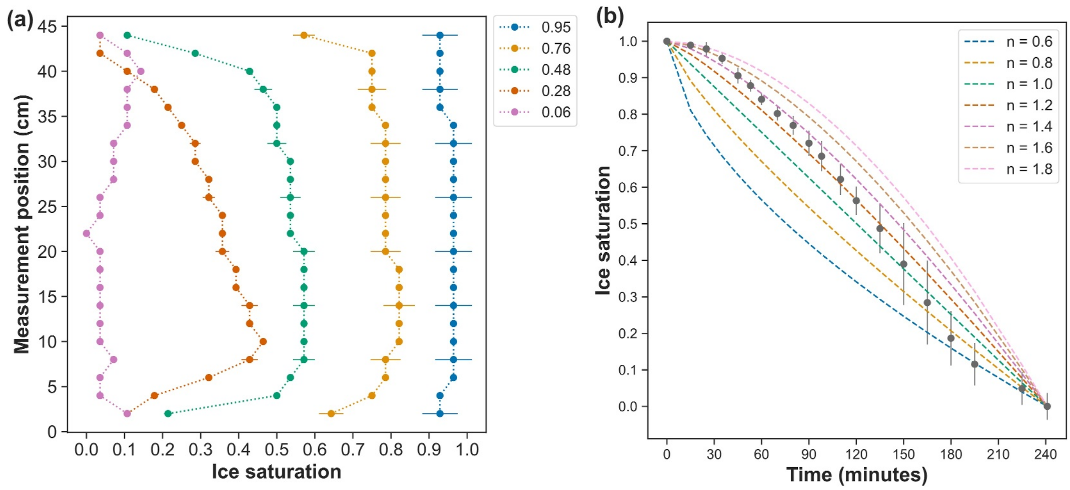

Figure 3. Ice saturation measurement using the microwave imaging setup during melting at 19°C (room temperature). (a) A representative subset of ice distribution along the sample core at various saturations, taken at 35, 80, 135, 165, and 225 min. Readings are taken every 2 cm along the sample, excluding the measurements near the top (50 cm) and bottom (0 cm) due to the interference from the polyvinyl chloride end caps. The legend values represent the average ice saturation of the entire sample. (b) Ice saturation (averaged throughout the core) against melting time, with n representing an empirical parameter.

To determine the empirical parameter n, we considered two things: the best fit of experimental data to the modeled results using the objective function (Equation 2, with results shown in Table 2) and how well the predicted experimental values at $S_i = 1$ (based on regression models) fit with the modeled results.

We found that the experimental velocities aligned best with the models using $n = 1.1–1.3$ (Figure 4a). In Supporting Information S1, we show that $n < 1.1$ overestimates velocities at $S_i = 1$ but matches the attenuation, while $n > 1.3$ underestimates velocities at $S_i = 1$ and leads to significant deviations in attenuation at $S_i > 0.6$. From the microwave data, we calculated $n = 1.2 \pm 0.1$ (Figure 3b), which is consistent with our model fits. Thus, we adopted $n = 1.2$ for the remainder of the discussions (see in Supporting Information S1 for full comparisons between the experimental results and model predictions).

3.2. Acoustic Properties of Ice-Bearing Sediment During the Ice-Melting Process

Velocity decreases with decreasing ice saturation, showing similar values for both samples, although Sample 2 exhibits a slightly lower velocity (by ∼1%) between $S_i = 0.2–0.7$ (Figure 5a). Velocity drops rapidly when $S_i > 0.5$ and decreases gradually as it approaches the fully melted state ($S_i = 0$). In contrast, attenuation generally increases with decreasing ice saturation, especially at higher ice saturations ($S_i = 0.4–0.9$), then increases more slowly at lower saturation. Both samples exhibit similar attenuation, with variations observed at $S_i < 0.2$, likely associated with variable ice distribution. The rates of change in velocity and attenuation confirm that ice saturation significantly affects both properties at higher saturation ($S_i > 0.5$), consistent across both samples, although attenuation analysis shows more variation (Figure 5b).

Table 2
Calculation of Objective Function to Compare Experimental and Modeled Velocity and Attenuation

	Objective function at $n =$				
Model	1	1.1	1.2	1.3	1.4
HBES–Voigt	0.38	0.36	0.35	0.36	0.38
HBES–Brie	0.52	0.51	0.50	0.53	0.57
HBES–Reuss	0.68	0.65	0.65	0.68	0.72
LeClaire	0.48	0.49	0.50	0.49	0.47

Note. A lower value indicates a better fit.

Using the regression models, we capture the non-linear response of velocity and attenuation during the melting process. We used third-degree polynomial models for both data sets. The models capture the trend fairly well at most saturation levels with R^2 (or the coefficient of determination) values of 0.98 for velocity and 0.93 for attenuation, indicating the models account for 98% and 93% of the experimental data variance. Increasing the polynomial degree did not significantly improve the fit.

The two samples show that velocity is only weakly frequency-dependent at all saturations but varies more significantly at higher ice saturations (Figure 6a), likely due to ice/water distribution effects. On average, velocity increases with frequency by ∼3% over the 3.2–20 kHz bandwidth, with the highest increase (∼6%) at $S_i > 0.9$. However, at $S_i \sim 0.7$, velocity tends to decrease

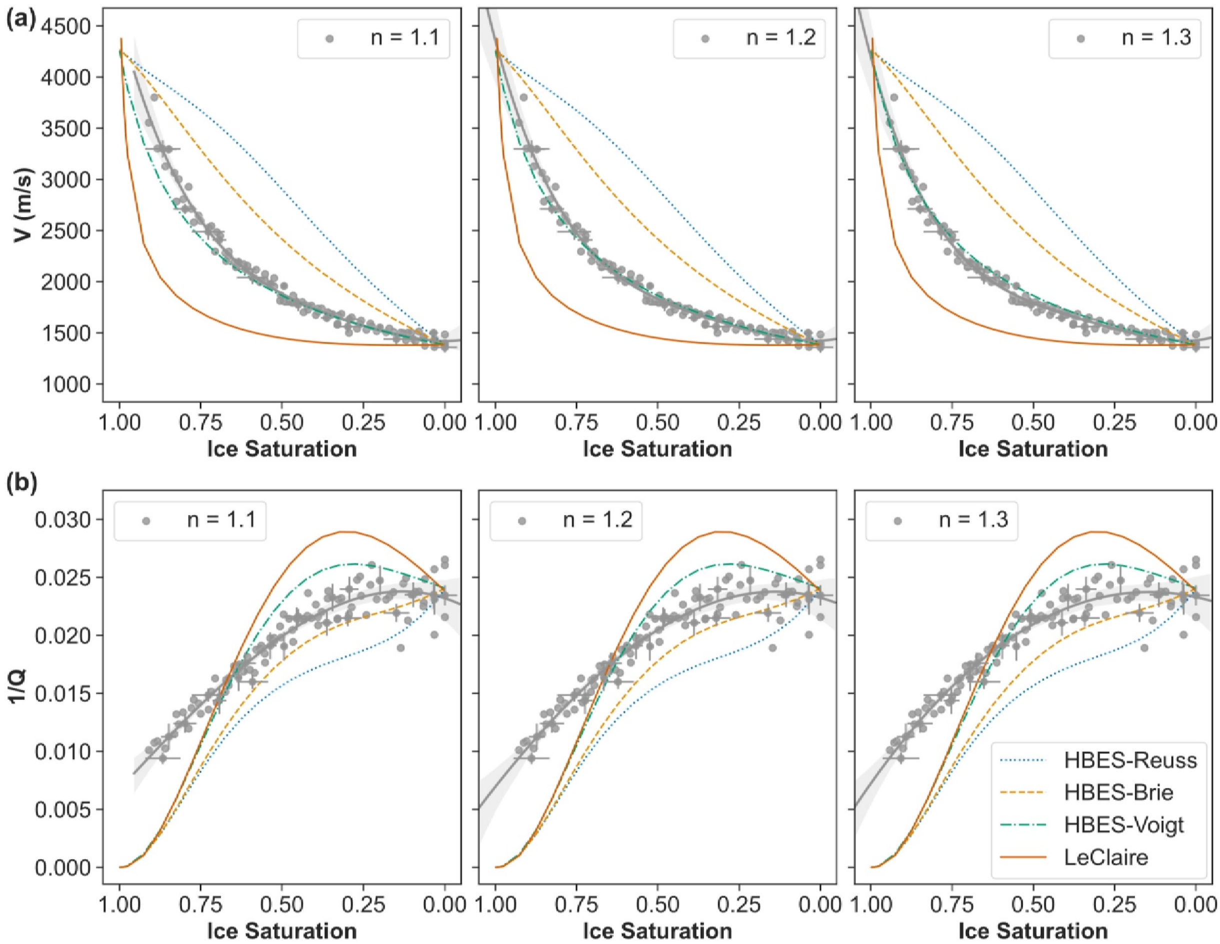

Figure 4. Empirical parameter (n) fitting of measured data (gray dots) of (a) velocity (V) and (b) attenuation ($1/Q$) to hydrate-bearing effective sediment (HBES) with Reuss, Brie, and Voigt approximations and LeClaire models. Gray solid lines represent the respective regression models to each data set with R^2 of 0.98 and 0.93 for velocity and attenuation, respectively. Cross error bars are shown at every 0.05 decrement of ice saturation (S_i).

with frequency, showing a ~5% decline over the same bandwidth. Note that we determined the cut-off frequency (3.2 kHz) to ensure that at least half of the wavelength should propagate through the sample (0.5 m in length) to provide accurate measurements. At 1.6–2.4 kHz, the half-wavelengths at high saturation for both samples are ~0.63–0.69 m, longer than the sample. At 3.2 kHz, the half-wavelengths are ~0.44–0.47 m, shorter than the sample, thus fulfilling the requirements.

Attenuation is more sensitive to frequency, especially above 8 kHz in the high saturation range (Figure 6b). Significant attenuation dips occur around 10–12 kHz at low saturation ($S_i \sim 0$–0.3) and around 17–19 kHz at intermediate to high saturation ($S_i \sim 0.5$–0.7) in both samples. The variations in attenuation, particularly at higher frequencies, can be attributed to patchiness or heterogeneous ice distribution (Matsushima et al., 2016). This observation is supported by the fact that the sensitivity of attenuation to frequency increases with the ice melting, showing consistent patterns across both samples. The wavelengths at these frequencies are below 0.1 m, indicating patchiness on a similar scale. Similar variations near fully melted conditions have also been observed in water-saturated sediment studies at full saturation (e.g., Dvorkin & Nur, 1998; Tserkovnyak & Johnson, 2002).

The similarity in velocity and attenuation values and patterns across both samples demonstrates the consistency in sample preparation and measurements, thereby validating the basis for further analysis. We used correlation analysis to explore how velocity and attenuation relate to ice saturation at different frequencies, especially due to the pulse tube's ability to measure a range of frequencies (Figure 6c).

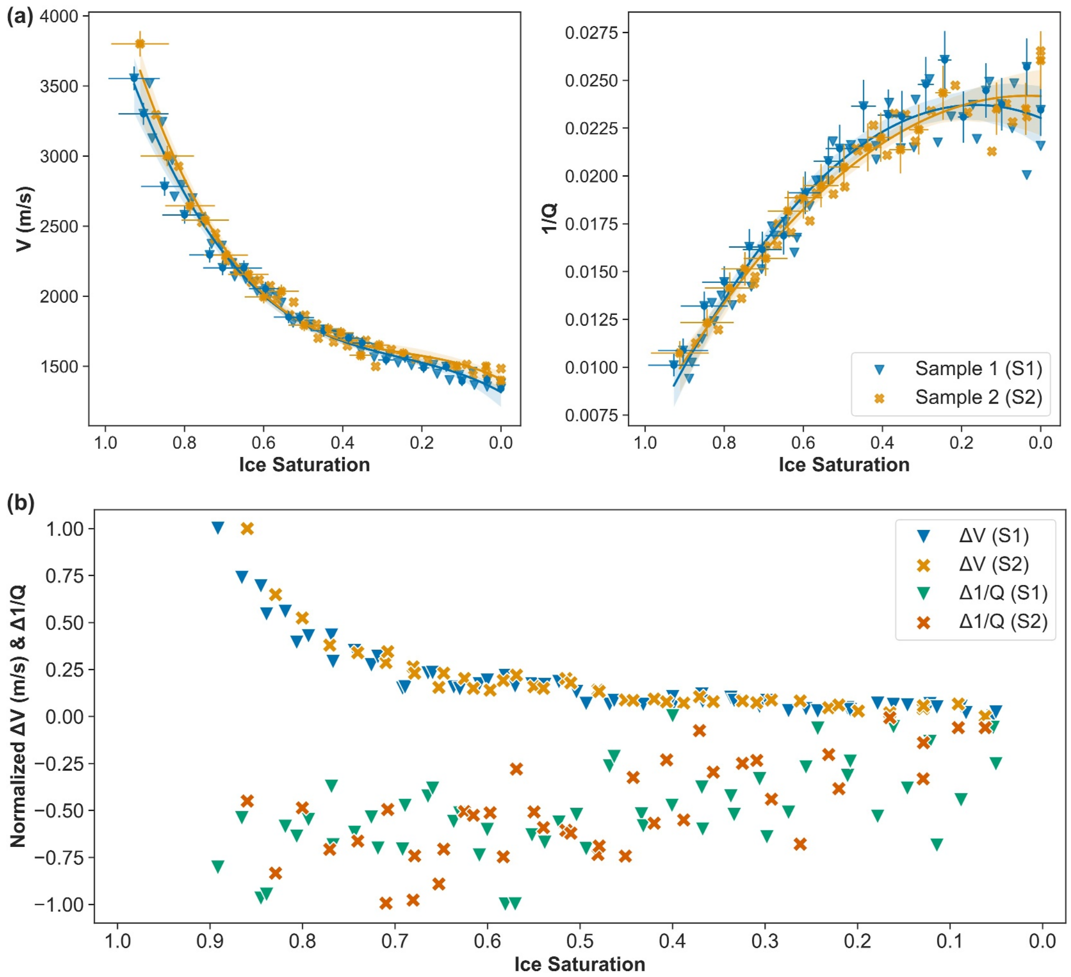

Figure 5. (a) Variations in velocity (V) and attenuation ($1/Q$) across ice saturations during melting at 10 kHz and 2.5 MPa. Samples 1 and 2 are prepared similarly with 100 μm Leighton Buzzard sand (porosity of 0.392 and 0.391). Solid lines represent regression models with R^2 of 0.98 and 0.93 for velocity and attenuation data sets, respectively. Cross error bars at every 0.05 decrement of ice saturation (S_i) reflect ~6% and ~7% uncertainties for Samples 1 and 2, associated with the saturation process, likely due to non-connected porosity and possible volumetric expansion. (b) Rate of changes of velocity and attenuation with decreasing S_i, normalized to their values at $S_i = 0$. Positive values indicate a decrease and negative values indicate an increase in acoustic properties with decreasing S_i.

Velocity strongly correlates with changes in ice saturation, with correlation values mainly above 0.85, especially at frequencies above 4 kHz. The correlation values are statistically significant for the entire frequency range, exceeding the 99% confidence line. Both samples show similar correlation values, with minor differences observed at frequencies below 4 kHz, which are mainly under the cut-off frequency of 3.2 kHz.

Attenuation also strongly correlates with changes in ice saturation, albeit negatively. Unlike velocity, correlation values for attenuation are higher at the lower frequency band (~2–9 kHz), exceeding the 99% confidence line. At frequencies above 10 kHz, correlations are mainly significant with 90% confidence. The weakest correlation is near the highest frequency band (>19 kHz). Correlation values for attenuation in both samples are similar but less converged than those for velocity, with higher values observed in Sample 2, particularly at lower frequencies.

We selected velocity and attenuation at four representative frequencies—3.2, 12.8, 16.8, and 20 kHz—to explore their correlation levels, spanning both below and above the 90% and 99% confidence thresholds (Figure 7). Figures for all frequencies can be found in (Figure S3 in Supporting Information S1), which shows consistency across both samples at all frequencies. This analysis is more relevant to attenuation because of its complex variation with frequency, unlike velocity which shows similar correlation values across the frequencies.

Figure 6. Variations in (a) velocity and (b) attenuation in frequency spectra at selected ice saturation levels (shown in legends) for Sample 1 and 2. Error bars are shown at each frequency at all saturations. Some error bars are not visible due to smaller than the data points. (c) Correlation values of velocity and attenuation with ice saturation across the frequency band for both samples. V and 1/Q represent velocity and attenuation, and S1 and S2 represent Samples 1 and 2.

Attenuation initially increases with decreasing ice saturation until $S_i \sim 0.4$ for both samples. Beyond this saturation level, attenuation varies differently at each frequency (Figure 7b). At 3.2 kHz (99% confidence level), attenuation continues to increase. At 12.8 kHz, differences between the samples are pronounced, with Sample 1 showing more variation than Sample 2. Despite the similar correlation values above the 99% confidence line, we observed differences at $S_i \sim 0.3$. At 16.8 kHz (90% confidence level), attenuation remains constant in average with decreasing ice saturation from $S_i \sim 0.5$ to 0. Sample 1 shows more variation than Sample 2, but the trends are similar. At 20 kHz, where correlations do not reach the 90% confidence cut-off, trends differ between samples. In

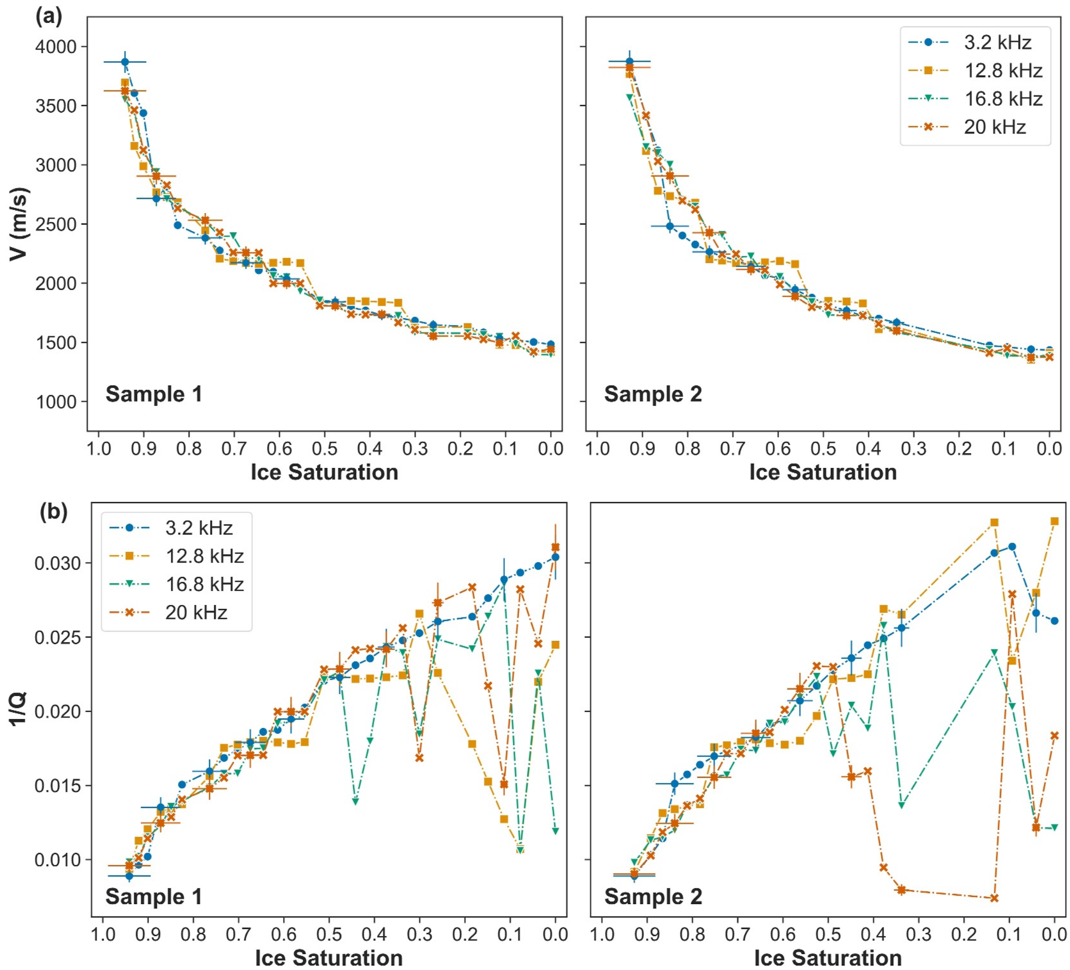

Figure 7. Variations in (a) velocity and (b) attenuation with ice saturations during the melting process of both samples at the selected frequency of 3.2, 12.8, 16.8, and 20 kHz. Cross error bars are shown at every 0.1 decrement of ice saturation (S_i).

Sample 1, attenuation increases until $S_i \sim 0.2$ before dipping significantly and stabilizing up to $S_i = 0$. In contrast, the attenuation of Sample 2 decreases from $S_i \sim 0.5$ to 0.3, stabilizes from $S_i \sim 0.3$ to 0.1, and then increases again up to $S_i = 0$.

The analysis highlights the importance of selecting an appropriate range of frequencies to accurately capture frequency-dependent behaviors within ice-bearing sediments. Velocity shows similar sensitivity to changes in ice content across all frequencies. However, attenuation is more sensitive to changes in ice content at higher frequencies due to smaller wavelengths that approach the size of the heterogeneities. At lower frequencies, attenuation shows a steady, predictable change with ice content because longer wavelength perceives the medium as homogeneous, unlike higher frequencies, where the wavelengths are comparable to the heterogeneities and show their presence more clearly.

Understanding these mechanisms at the correct frequencies enhances our ability to monitor and predict changes in ice-bearing sediments, which has broader implications for fields like quantifying ice content in permafrost and its monitoring (e.g., Hilbich et al., 2022; Lin et al., 2018). For example, in sub-bottom profilers, higher frequencies may lead to increased energy scattering and reduced sub-bottom penetration in areas with partially melted seabed permafrost.

4. Modeling Insight

4.1. Three-Phase Models

Both experimental data and model predictions show that velocity decreases with decreasing ice saturation, although at different rates (Figure 8a). The models represent a three-phase approach to predicting the velocity and attenuation, with the LeClaire model representing the least uniform ice distribution (i.e., patchy ice distribution), while the HBES-Reuss model represents the most uniform ice distribution. The HBES-Brie model represents conditions between both of these end-member predictions. The LeClaire model predicts the fastest velocity decrease at $S_i = 1.0$ to ~ 0.8, followed by HBES with Voigt, Brie, and Reuss approximations, respectively. Our data aligns well with the HBES–Voigt model, which may suggest moderate to patchy ice distribution, though at $S_i < 0.5$, the data sometimes falls between the HBES–Voigt and LeClaire models. This pattern could suggest that at this saturation range, the system behaves like a three-phase system with sufficient ice and water within the sand matrix. However, at higher ice saturations, ice grains may interlock, thus limiting relative motion between the three phases, which was also found by Sahoo et al. (2019) in hydrate-bearing sediment cases, which are similar in characteristics to our ice study.

Attenuation predictions from the models show various patterns. The LeClaire and HBES–Voigt models predict an increase in attenuation as saturation decreases from $S_i = 1.0$ to 0.3, followed by a decrease up to $S_i = 0$, with LeClaire's prediction showing a higher rate of decrease. Meanwhile, HBES–Brie and Reuss models mainly show a continued increase in attenuation as saturation decreases. LeClaire's model shows the highest attenuation at $S_i = 0.3$ and the lowest at $S_i = 1.0$, mainly due to squirt flow loss (Guerin & Goldberg, 2005). For HBES predictions, the lowest attenuation is observed at $S_i = 1.0$, while the highest at $S_i = 0.3$ for Voigt, and at $S_i = 0$ for Brie and Reuss approximations. Our experimental results fall between HBES–Voigt and Brie predictions, particularly at $S_i < 0.6$. At $S_i > 0.6$, the experimental attenuation is higher than the predictions.

Based on the objective function comparison, we chose the HBES model with Voigt approximation for further discussion, supported by Best et al. (2013), who found that LeClaire's model works better for S-waves rather than P-waves, which we used in this study.

4.2. Ice Formation Morphology

We investigated how the location of ice formation affects velocity and attenuation using the HBES model (Figure 8b). This model can consider different morphologies, a term commonly used in hydrate formation, where ice forms either as part of the pore fluid (PF) or as cementing ($C = 1 - PF$) that strengthens the sediment matrix. We tested PF concentrations from 0 to one in increments of 0.1, focusing on the figures relevant to our experimental data. Results from the complete simulation are provided in Supporting Information S1.

Velocity decreases with decreasing ice saturation, with similar trends across PF scenarios. Higher PF concentrations generally show lower velocity, but the differences are not significant, particularly at intermediate saturations ($S_i = 0.8$ to 0.4). Higher PF concentrations show a higher velocity decrease with decreasing ice saturation, particularly at $S_i > 0.8$. Experimental velocities align well with the 1.0 PF scenario, particularly at $S_i > 0.6$, and intersect with lower PF scenarios at $S_i = 0.6$ to 0.4. However, the velocity differences due to different PF concentrations are still within the variation of the experimental velocity, particularly at the intermediate saturation, because trend-wise, the experimental velocity matches the higher PF concentration, particularly for the high decrease rate at high ice saturation ($S_i = 1.0$ to 0.8).

Attenuation in all scenarios increases with decreasing ice saturation, with different rates for each PF concentration scenario. Lower PF concentration leads to lower attenuation. Changes in attenuation across PF concentrations are caused by changes in viscous drag between the solids (i.e., ice grains) and global fluid flow as per Biot's attenuation mechanism (Marín-Moreno et al., 2017). Experimental attenuation fits better with the higher PF scenario; however, at $S_i < 0.6$, the experimental attenuation varies. Meanwhile, at $S_i > 0.6$, the experimental attenuation intersects with the predicted attenuation with lower PF concentrations ($PF = 0.6$–0.9), which may suggest that some of the ice may form around the sand grain rather than fully in the pore fluid.

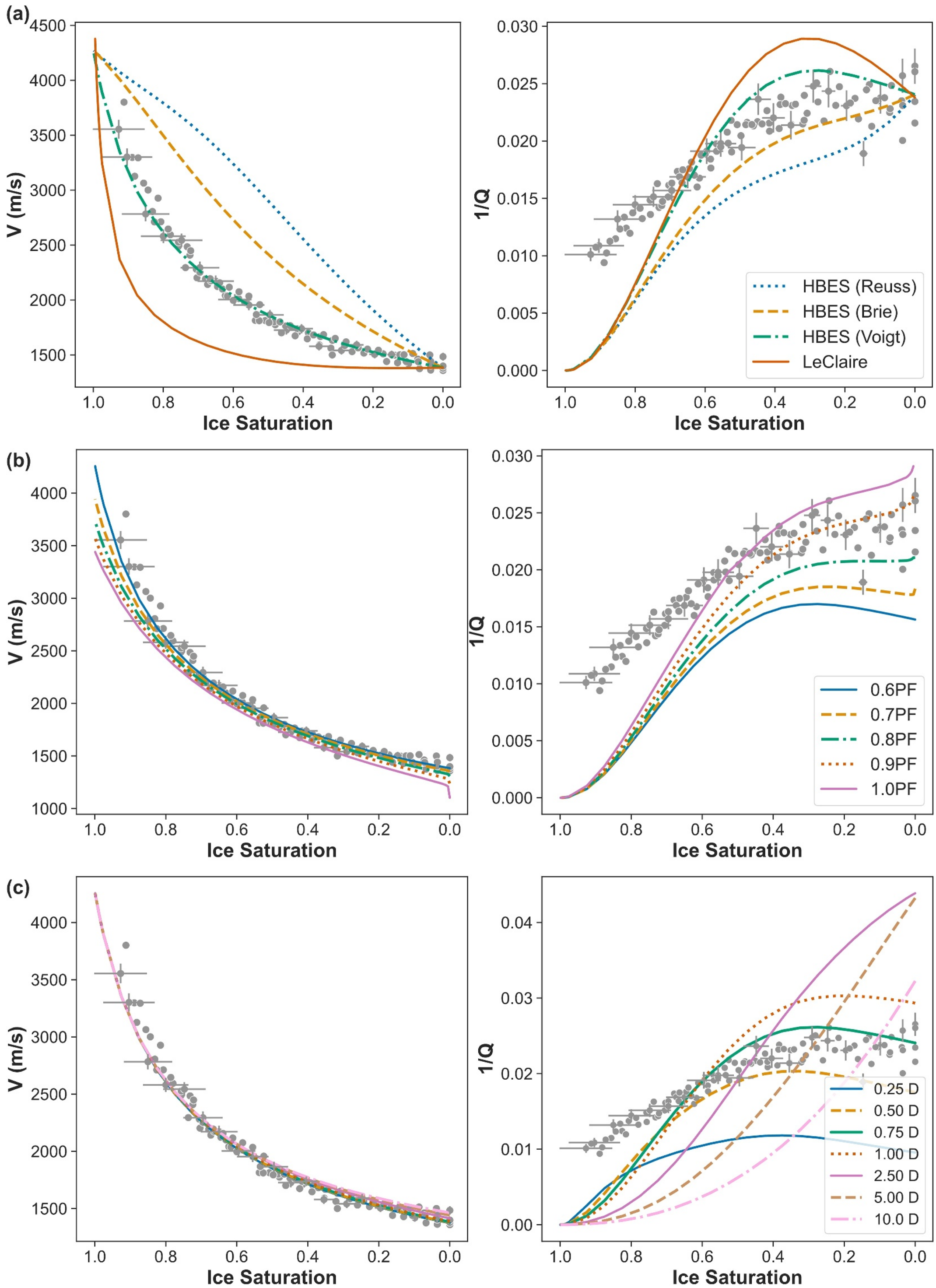

Figure 8. Comparison of velocity (left) and attenuation (right), at 10 kHz and 2.5 MPa effective pressure: (a) against HBES (with various effective fluid bulk modulus approximations) and LeClaire models across ice saturation during the melting process, (b) against HBES model with selected pore-filling concentrations across ice saturation during the melting process, and (c) against HBES model with various permeability values across ice saturation during the melting process. Cross error bars for the experimental data set are shown at every 0.05 decrement of ice saturation (S_i).

4.3. Permeability

Velocity barely varies with changes in the sediment frame's permeability across all ice saturation (Figure 8c). At $S_i = 0$, lower permeability predicts lower velocities with about a difference of ~50 ms^{-1} between the 0.25 and 10 Darcy (D) scenarios. At $S_i = 1.0$, velocities from all permeability scenarios converge to a similar value. Therefore, lower permeability predicts a higher decrease in velocity with ice saturation.

At permeabilities below 1 D, attenuation increases with decreasing ice saturation up to $S_i \sim 0.4$, then slightly decreases up to $S_i = 1$. For higher permeabilities, attenuation increases continuously up to $S_i = 1$. The peak of attenuation shifts to lower ice saturation as permeability increases up to 2.5 D. All permeability scenarios underpredict attenuation at $S_i > 0.6$ when compared to experimental attenuation. However, experimental attenuation falls between the 0.5 and 0.75 D predictions at $S_i < 0.6$. This range is within the permeability values of ice-bearing sand in permafrost environments, which range approximately from 0.05 to 10 D (Kleinberg & Griffin, 2005; Lacelle et al., 2022). The permeability value represents the permeability of the sediment frame without ice ($S_i = 0$). At higher ice saturations, permeability is expected to decrease due to reduced pore spaces caused by ice formation. In contrast, at lower ice saturations, permeability is expected to increase as more open spaces become available, leading to higher attenuation due to global fluid flow. These changes are particularly significant at $S_i > 0.4$, which may indicate a shift in ice morphology around this saturation level (see in Supporting Information S1).

4.4. Gas Saturation and Bubble Size

Predicted velocity changes slightly with varying gas saturation (S_g) at different ice saturations (Figure 9a). The most significant difference occurs at maximum ice saturation, where lower gas saturation generates higher velocity. On average, velocities at lower gas saturations ($S_g < 0.025$) are similar, while higher gas saturation produces a visibly lower velocity. Our experimental data best fits the predicted velocity without any gas present ($S_g = 0$).

Predicted attenuation differs in value with a similar trend with varying gas saturation at different ice saturation. Attenuation increases with gas saturation, and the variations are more pronounced than those in velocity. The increase in attenuation due to increased gas saturation aligns with our experimental attenuation. At $S_i = 0.6$, experimental attenuation intersects with the predicted attenuation at $S_g = 0$, then at $S_i > 0.8$, experimental attenuation intersects with the predicted attenuation at $S_g > 0.01$. This may suggest that high experimental attenuation, particularly at $S_i > 0.6$, could be due to a small concentration of gas. At high ice saturation, most pore water is frozen; therefore, leaving gas within the pores. However, as the ice melts, more pore water becomes available, increasing the concentration gradient between water and gas, thus increasing the gas solubility, making the gas easier to dissolve into water, particularly under high effective pressure (Sander, 2015).

We also explored how gas bubble size affects velocity and attenuation. To determine the appropriate bubble size range, we calculated the pore throat size (a) for our samples. Stoll (1974) found that pore throat sizes typically range from one-sixth to one-seventh of the mean grain diameter (d). Meanwhile, Hovem and Ingram (1979) provided the formula as follows: $a = \varnothing d/[3(1 - \varnothing)]$, where $\varnothing$ is porosity. Using both methods, we calculated the pore throat size between 0.014–0.023 mm.

We tested four gas bubble sizes to represent microbubble (0.01 mm), fine bubble (0.1 mm), medium bubble (1 mm), and coarse bubble (10 mm) (Figure 9b). Predicted velocity remains consistent across all bubble sizes, and attenuation shows no significant change for bubble radii below 1 mm. A significant change in predicted attenuation occurs at the bubble size of 10 mm, however, it exceeds both our experimental attenuation and the calculated pore throat size. Overall, the experimental results align with bubble sizes no larger than 0.1 mm, which explains the lack of noticeable gas bubble resonance effects on attenuation for the predicted bubble sizes (Gong et al., 2010).

5. Discussion

Ice distribution affects the acoustic attributes of sediments; but also, its location with respect to grains within the porous medium. This study shows that as the ice melts, velocity decreases while attenuation increases, which agrees with previous ice melting/permafrost thawing studies (e.g., Matsushima et al., 2016; Yang et al., 2021). We observe that velocity is more sensitive to ice saturation (S_i) changes in the high S_i range ($S_i > 0.5$). This effect

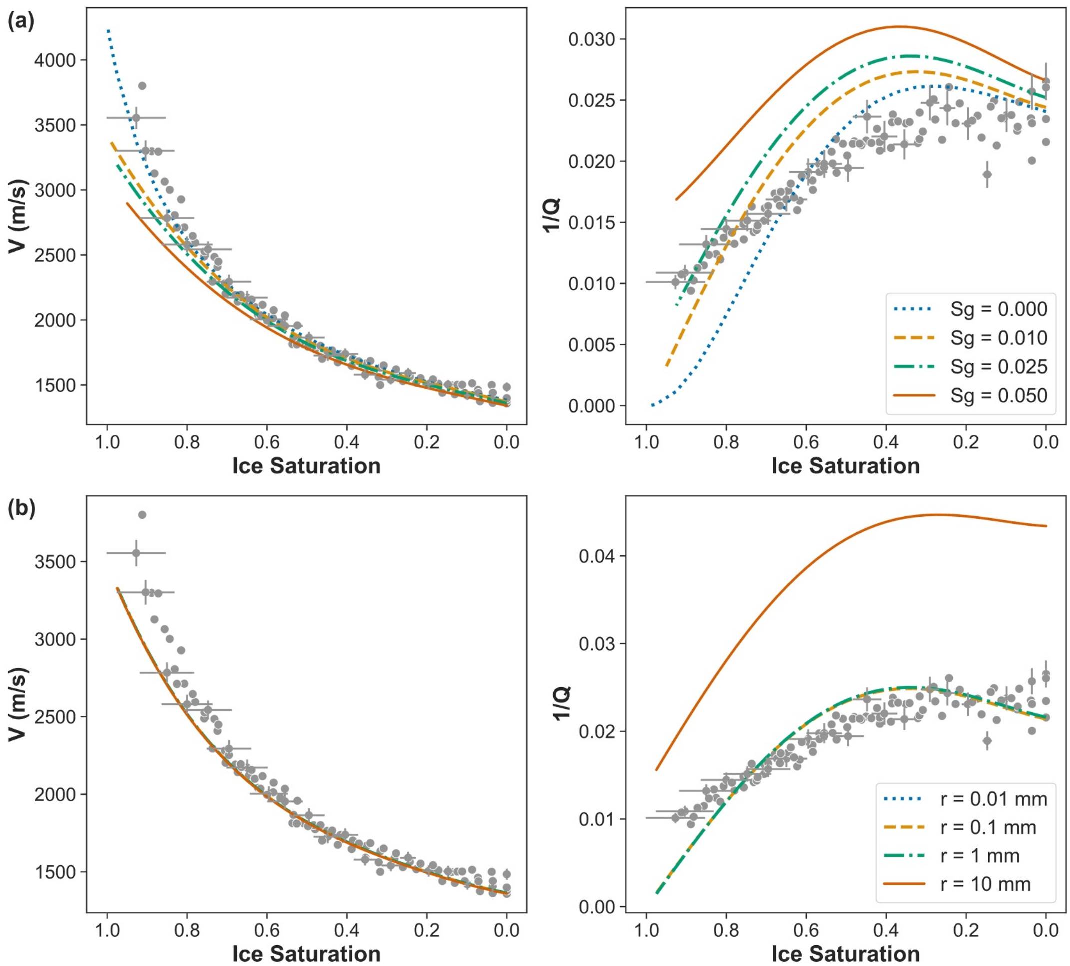

Figure 9. Comparison of velocity (left) and attenuation (right), at 10 kHz and 2.5 MPa effective pressure, against HBES model with various (a) gas saturation (S_g) with a gas bubble size of 0.01 mm, and (b) gas bubble size (r) with $S_g = 0.025$, across ice saturation during the melting process. The $r = 0.01$–0.1 mm curves are not shown due to having similar values with the $r = 1$ mm curve. Gray dots represent the experimental data, and dashed lines represent the models (as shown in the legend). Cross error bars for the experimental data set are shown at every 0.05 decrement of ice saturation (S_i).

might be related to ice forming at grain contact above a certain S_i, leading to combined cementation and pore-clogging phenomena that, in turn, increased the stiffness of the sand frame. At low saturations, the ice effect on velocity may be less pronounced due to inclusion in the pore fluid, so changes in velocity are less significant.

On the other hand, attenuation increases with ice melting down to $S_i \sim 0.4$, then it stabilizes. At higher saturation, the introduction of water coexisting with ice increases viscous drag, thus increasing the attenuation. However, once the saturation reaches $S_i \sim 0.4$, further melting may not significantly change the fluid dynamics, as there is already enough water present to reach a steady state. In addition, at high frequencies (e.g., sonic frequencies), unrelaxed pores may contribute to attenuation (Cadoret et al., 1998; Mavko and Nolen-Hoeksema, 1994). Similar changes have been observed in the studies of ice-bearing and gas hydrate-bearing sediments (e.g., Li & Matsushima, 2024; Sahoo & Best, 2021). The sensitivity of both velocity and attenuation to ice content suggests that these parameters could be used to estimate ice content in the field, particularly at high saturation where both parameters are equally sensitive. Estimation can be performed through direct comparison with field measurements (e.g., well-log data) or enhanced by supervised machine learning (e.g., Bustamante et al., 2024; Singh et al., 2021), where laboratory data are used to train models to predict ice content from field measurements. However, a larger data set is needed to provide effective training and testing processes.

We have ensured that the measurements well capture the sample characteristics by considering its length (i.e., 0.5 m) relative to the sonic wavelength. However, our focus on a homogeneous sand pack may contrast with the field conditions where permafrost may be composed of sediments with varying grain sizes and lithologies. The volumetric expansion caused by melting ice could also affect the measurements. As ice melts and contracts, it may introduce errors in saturation estimation. In addition, there could still be some unfrozen water present after the freezing process in the form of thin water films (Dash et al., 1995; Watanabe & Mizoguchi, 2002). We have included error bars in our figures to address these potential issues.

These limitations suggest future research directions, such as investigating different sediment types, scaling up to field samples, and employing real-time monitoring to better understand ice and water distribution in the sample.

6. Conclusion

This study enhances the understanding of frequency-dependent acoustic behaviors in ice-bearing sands at sonic frequencies, addressing gaps in how P-wave velocity and attenuation respond to varying ice saturations, which is important for studying permafrost and gas hydrate stability, particularly in the light of climate change.

Our findings show that while P-wave velocity consistently correlates with ice saturation across all frequencies, attenuation demonstrates higher sensitivity at higher frequencies. This difference is important for selecting optimal frequencies for subsurface monitoring of ice-bearing sediments. By comparing experimental results with three-phase models, we identified that the HBES model with Voigt approximation better represents patchy ice distributions, providing a more accurate framework for interpreting field data.

These findings offer potential practical applications in improving geophysical survey designs for permafrost regions which may also deposit gas hydrates (incorporating potent greenhouse gases like methane), allowing more accurate estimations of ice content and sediment stability. Future studies could expand on these results by integrating field-scale data and refining models to account for complex pore fluid interactions, further improving the understanding of ice content in permafrost for monitoring purposes.

Data Availability Statement

The P-wave velocity and attenuation data set from the ice melting process is available at Sutiyoso, Sahoo, and North (2024).

Acknowledgments

Financial support from the Indonesian Endowment Fund for Education (Lembaga Pengelola Dana Pendidikan, LPDP) is gratefully acknowledged. We acknowledge funding from the UK Natural Environment Research Council for the acoustic pulse tube (Grant NE/J020753/1). Sahoo was supported by NOC RISC funding (Project No P11828).

References

Ahmed, N., Weibull, W. W., Quintal, B., Grana, D., & Bhakta, T. (2022). Frequency-dependent AVO inversion applied to physically based models for seismic attenuation. *Geophysical Journal International*, *233*(1), 234–252. https://doi.org/10.1093/gji/ggac461

Barriere, J., Bordes, C., Brito, D., Senechal, P., & Perroud, H. (2012). Laboratory monitoring of P waves in partially saturated sand. *Geophysical Journal International*, *191*(3), 1152–1170. https://doi.org/10.1111/j.1365-246X.2012.05691.x

Belogol'skii, V. A., Sekoyan, S. S., Samorukova, L. M., Stefanov, S. R., & Levtsov, V. I. (1999). Pressure dependence of the sound velocity in distilled water. *Measurement Techniques*, *42*(4), 406–413. https://doi.org/10.1007/BF02504405

Berryman, J. G. (1981). Elastic wave propagation in fluid-saturated porous media II. *Journal of the Acoustical Society of America*, *70*(6), 1754–1756. https://doi.org/10.1121/1.387193

Best, A. I., Priest, J. A., Clayton, C. R. I., & Rees, E. V. L. (2013). The effect of methane hydrate morphology and water saturation on seismic wave attenuation in sand under shallow sub-seafloor conditions. *Earth and Planetary Science Letters*, *368*, 78–87. https://doi.org/10.1016/j.epsl.2013.02.033

Biot, M. A. (1956). Theory of propagation of elastic waves in a fluid-saturated porous solid. II. Higher frequency range. *Journal of the Acoustical Society of America*, *28*(2), 179–191. https://doi.org/10.1121/1.1908241

Biot, M. A. (1962). Mechanics of deformation and acoustic propagation in porous media. *Journal of Applied Physics*, *33*(4), 1482–1498. https://doi.org/10.1063/1.1728759

Brie, A., Pampuri, F., Marsala, A. F., & Meazza, O. (1995). Shear sonic interpretation in gas-bearing sands. *Presented at the SPE Annual Technical Conference and Exhibition*, SPE-30595-MS. https://doi.org/10.2118/30595-MS

Bustamante, J., Fabien-Ouellet, G., Duchesne, M. J., & Ibrahim, A. (2023). Understanding seismic velocity variations of subsea permafrost: A sensitivity study. *Geophysics*, *88*(5), R655–R669. https://doi.org/10.1190/geo2022-0568.1

Bustamante, J., Fabien-Ouellet, G., Duchesne, M. J., & Ibrahim, A. (2024). Deep-learning viscoelastic seismic inversion for mapping subsea permafrost. *Geophysics*, *89*(4), R339–R353. https://doi.org/10.1190/geo2022-0759.1

Cadoret, T., Mavko, G., & Zinszner, B. (1998). Fluid distribution effect on sonic attenuation in partially saturated limestones. *Geophysics*, *63*(1), 154–160. https://doi.org/10.1190/1.1444308

Chang, X., Liu, W., Zuo, G., Dou, Y., & Li, Y. (2021). Research on ultrasonic-based investigation of mechanical properties of ice. *Acta Oceanologica Sinica*, *40*(10), 97–105. https://doi.org/10.1007/s13131-021-1890-3

Chotiros, N. P. (1995). Biot model of sound propagation in water-saturated sand. *Journal of the Acoustical Society of America*, *97*(1), 17–214. https://doi.org/10.1121/1.412304

Dash, J. G., Fu, H., & Wettlaufer, J. S. (1995). The premelting of ice and its environmental consequences. *Reports on Progress in Physics*, *58*(1), 115–167. https://doi.org/10.1088/0034-4885/58/1/003

Dobiński, W. (2020). Permafrost active layer. *Earth-Science Reviews*, *208*, 103301. https://doi.org/10.1016/j.earscirev.2020.103301

Dubbelday, P. S., & Capps, R. N. (1984). Interpretation of sample wave speed measured in an impedance tube. *Journal of the Acoustical Society of America*, *76*(3), 964–967. https://doi.org/10.1121/1.391217

Dvorkin, J., & Nur, A. (1998). Acoustic signatures of patchy saturation. *International Journal of Solids and Structures*, *35*(34–35), 4803–4810. https://doi.org/10.1016/S0020-7683(98)00095-X

Falcon-Suarez, I. H., Dale, M., & Marin-Moreno, H. (2024). Experimental study of geophysical and transport properties of salt rocks in the context of underground energy storage. *Geophysical Prospecting*, *72*(5), 2032–2048. https://doi.org/10.1111/1365-2478.13516

Gabitto, J. F., & Tsouris, C. (2010). Physical properties of gas hydrates: A review. *Journal of Thermodynamics*, *2010*, 1–12. https://doi.org/10.1155/2010/271291

Gong, Y., Cabodi, M., & Porter, T. (2010). Pressure-dependent Resonance Frequency for Lipid-coated Microbubbles at Low Acoustic Pressures.

Guerin, G., & Goldberg, D. (2002). Sonic waveform attenuation in gas hydrate-bearing sediments from the Mallik 2L-38 research well, Mackenzie Delta, Canada. *Journal of Geophysical Research*, *107*(B5). https://doi.org/10.1029/2001JB000556

Guerin, G., & Goldberg, D. (2005). Modeling of acoustic wave dissipation in gas hydrate-bearing sediments: Acoustic wave dissipation. *Geochemistry, Geophysics, Geosystems*, *6*(7), Q07010. https://doi.org/10.1029/2005GC000918

Helgerud, M. B., Waite, W. F., Kirby, S. H., & Nur, A. (2009). Elastic wave speeds and moduli in polycrystalline ice Ih, sI methane hydrate, and sII methane-ethane hydrate. *Journal of Geophysical Research*, *114*(B2), B02212. https://doi.org/10.1029/2008JB006132

Hilbich, C., Hauck, C., Mollaret, C., Wainstein, P., & Arenson, L. U. (2022). Towards accurate quantification of ice content in permafrost of the Central Andes – Part 1: Geophysics-based estimates from three different regions. *The Cryosphere*, *16*(5), 1845–1872. https://doi.org/10.5194/tc-16-1845-2022

Hjort, J., Streletskiy, D. A., Doré, G., Wu, Q., Bjella, K., & Luoto, M., (2022). Impacts of permafrost degradation on infrastructure *3*, 24–38. https://doi.org/10.1038/s43017-021-00247-8

Hovem, J. M., & Ingram, G. D. (1979). Viscous attenuation of sound in saturated sand. *Journal of the Acoustical Society of America*, *66*(6), 1807–1812. https://doi.org/10.1121/1.383653

James, S. R., Minsley, B. J., McFarland, J. W., Euskirchen, E. S., Edgar, C. W., & Waldrop, M. P. (2021). The biophysical role of water and ice within permafrost nearing collapse: Insights from novel geophysical observations. *JGR Earth Surface*, *126*(6), e2021JF006104. https://doi.org/10.1029/2021JF006104

Kang, S., Jin, Y. K., Jang, U., Duchesne, M. J., Shin, C., Kim, S., et al. (2021). Imaging the P-wave velocity structure of arctic subsea permafrost using laplace-domain full-waveform inversion. *JGR Earth Surface*, *126*(3), e2020JF005941. https://doi.org/10.1029/2020JF005941

Kleinberg, R. L., & Griffin, D. D. (2005). NMR measurements of permafrost: Unfrozen water assay, pore-scale distribution of ice, and hydraulic permeability of sediments. *Cold Regions Science and Technology*, *42*(1), 63–77. https://doi.org/10.1016/j.coldregions.2004.12.002

Knight, R., & Nolen-Hoeksema, R. (1990). A laboratory study of the dependence of elastic wave velocities on pore scale fluid distribution. *Geophysical Research Letters*, *17*(10), 1529–1532. https://doi.org/10.1029/GL017i010p01529

Kolsky, H. (1964). Stress waves in solids. *Journal of Sound and Vibration*, *1*, 88–110. https://doi.org/10.1016/0022-460X(64)90008-2

Kvenvolden, K. A. (1988). Methane hydrate — A major reservoir of carbon in the shallow geosphere? *Chemical Geology*, *71*(1–3), 41–51. https://doi.org/10.1016/0009-2541(88)90104-0

Kvenvolden, K. A. (1993). Gas hydrates-geological perspective and global change. *Reviews of Geophysics*, *31*(2), 173–187. https://doi.org/10.1029/93RG00268

Lacelle, D., Fisher, D. A., Verret, M., & Pollard, W. (2022). Improved prediction of the vertical distribution of ground ice in Arctic-Antarctic permafrost sediments. *Commun Earth Environ*, *3*(1), 31. https://doi.org/10.1038/s43247-022-00367-z

Leclaire, P., Cohen-Ténoudji, F., & Aguirre-Puente, J. (1994). Extension of Biot's theory of wave propagation to frozen porous media. *Journal of the Acoustical Society of America*, *96*(6), 3753–3768. https://doi.org/10.1121/1.411336

Leurer, K. C. (1997). Attenuation in fine-grained marine sediments: Extension of the Biot-Stoll model by the "effective grain model" (EGM). *Geophysics*, *62*(5), 1465–1479. https://doi.org/10.1190/1.1444250

Leurer, K. C., & Brown, C. (2008). Acoustics of marine sediment under compaction: Binary grain-size model and viscoelastic extension of Biot's theory. *Journal of the Acoustical Society of America*, *123*(4), 1941–1951. https://doi.org/10.1121/1.2871839

Li, B., & Matsushima, J. (2024). Influence of ice properties on wave propagation characteristics in partially frozen soils and rocks: A temperature-dependent rock-physics model. *Geophysics*, *89*(5), MR281–MR295. https://doi.org/10.1190/geo2023-0694.1

Lin, Z., Pan, H., Fang, H., Gao, W., & Liu, D. (2018). High-altitude well log evaluation of a permafrost gas hydrate reservoir in the Muli area of Qinghai, China. *Scientific Reports*, *8*(1), 12596. https://doi.org/10.1038/s41598-018-30795-x

Marín-Moreno, H., Sahoo, S. K., & Best, A. I. (2017). Theoretical modeling insights into elastic wave attenuation mechanisms in marine sediments with pore-filling methane hydrate: Hydrate-Bearing Effective Sediment Model. *Journal of Geophysical Research: Solid Earth*, *122*, 1835–1847. https://doi.org/10.1002/2016JB013577

Matsushima, J., Suzuki, M., Kato, Y., Nibe, T., & Rokugawa, S. (2008). Laboratory experiments on compressional ultrasonic wave attenuation in partially frozen brines. *Geophysics*, *73*(2), 1MA–Z29. https://doi.org/10.1190/1.2827214

Matsushima, J., Suzuki, M., Kato, Y., & Rokugawa, S. (2016). Ultrasonic measurements of attenuation and velocity of compressional and shear waves in partially frozen unconsolidated sediment and synthetic porous rock. *Geophysics*, *81*(2), D141–D153. https://doi.org/10.1190/geo2015-0350.1

Mavko, G., & Nolen-Hoeksema, R. (1994). Estimating seismic velocities at ultrasonic frequencies in partially saturated rocks. *Geophysics*, *59*(2), 252–258. https://doi.org/10.1190/1.1443587

McCann, C., Sothcott, J., & Best, A. I. (2014). A new laboratory technique for determining the compressional wave properties of marine sediments at sonic frequencies and *in situ* pressures: Compressional wave properties of marine sediments. *Geophysical Prospecting*, *62*(1), 97–116. https://doi.org/10.1111/1365-2478.12079

McCutchan, A., & Johnson, B. (2022). Laboratory experiments on ice melting: A need for understanding dynamics at the ice-water interface. *JMSE*, *10*(8), 1008. https://doi.org/10.3390/jmse10081008

Murphy, W. F. (1982). *Effects of Microstructure and Pore Fluids on the Acoustic Properties of Granular Sedimentary Materials, Stanford Rock Physics Project report*. Stanford University.

North, L., & Best, A. (2015). An improved high-spectral resolution water filled impedance tube measurement method for marine sediment studies. In *Seabed and Sediment Acoustics 2015. Presented at the Seabed and Sediment Acoustics 2015, Institute of Acoustics, Bath*. https://doi.org/10.25144/18070

Oda, H., Nishizawa, S., Kusunose, K., & Hirata, T. (1990). Frequency-dependence of velocity and attenuation of elastic waves in granite under uniaxial compression. *Pure and Applied Geophysics*, *133*(1), 73–85. https://doi.org/10.1007/bf00876703

O'Hara, S. G. (1985). Influence of pressure, temperature, and pore fluid on the frequency-dependent attenuation of elastic waves in Berea sandstone. *Physical Review A*, *32*(1), 472–488. https://doi.org/10.1103/PhysRevA.32.472

Pearson, C. F., Halleck, P. M., McGuire, P. L., Hermes, R., & Mathews, M. (1983). Natural gas hydrate deposits: A review of in situ properties. *The Journal of Physical Chemistry A*, *87*(21), 4180–4185. https://doi.org/10.1021/j100244a041

Reuss, A. (1929). Berechnung der Fließgrenze von Mischkristallen auf Grund der Plastizitätsbedingung für Einkristalle. *Zeitschrift für Angewandte Mathematik und Mechanik*, *9*(1), 49–58. https://doi.org/10.1002/zamm.19290090104

Rubino, J. G., & Holliger, K. (2012). Seismic attenuation and velocity dispersion in heterogeneous partially saturated porous rocks: Mesoscopic effects and partial saturation. *Geophysical Journal International*, *188*(3), 1088–1102. https://doi.org/10.1111/j.1365-246X.2011.05291.x

Ruppel, C. D., & Kessler, J. D. (2017). The interaction of climate change and methane hydrates. *Reviews of Geophysics*, *55*(1), 126–168. https://doi.org/10.1002/2016RG000534

Sahoo, S. K., & Best, A. I. (2021). The influence of gas hydrate morphology on reservoir permeability and geophysical shear wave remote sensing. *JGR Solid Earth*, *126*(11), e2021JB022206. https://doi.org/10.1029/2021JB022206

Sahoo, S. K., North, L. J., Marín-Moreno, H., Minshull, T. A., & Best, A. I. (2019). Laboratory observations of frequency-dependent ultrasonic P-wave velocity and attenuation during methane hydrate formation in Berea sandstone. *Geophysical Journal International*, *219*(1), 713–723. https://doi.org/10.1093/gji/ggz311

Sander, R. (2015). Compilation of Henry's law constants (version 4.0) for water as solvent. *Atmospheric Chemistry and Physics*, *15*(8), 4399–4981. https://doi.org/10.5194/acp-15-4399-2015

Schumann, K., Stipp, M., Behrmann, J. H., Klaeschen, D., & Schulte-Kortnack, D. (2014). *P* and *S* wave velocity measurements of water-rich sediments from the nankai trough, Japan: P- and S-wave velocity measurements. *Journal of Geophysical Research: Solid Earth*, *119*(2), 787–805. https://doi.org/10.1002/2013JB010290

Schuur, E. A. G., McGuire, A. D., Schädel, C., Grosse, G., Harden, J. W., Hayes, D. J., et al. (2015). Climate change and the permafrost carbon feedback. *Nature*, *520*(7546), 171–179. https://doi.org/10.1038/nature14338

Selfridge, A. R. (1985). Approximate material properties in isotropic materials. *IEEE Transactions on Sonics and Ultrasonics*, *32*(3), 381–394. https://doi.org/10.1109/T-SU.1985.31608

Simmons, G. (1965). Single Crystal Elastic Constants and Calculated Aggregate Properties 274.

Singh, H., Seol, Y., & Myshakin, E. M. (2021). Prediction of gas hydrate saturation using machine learning and optimal set of well-logs. *Computational Geosciences*, *25*(1), 267–283. https://doi.org/10.1007/s10596-020-10004-3

Stoll, R. D. (1974). Acoustic waves in saturated sediments. In *Presented at the Physics of Sound in Marine Sediments* (pp. 19–39).

Stoll, R. D., & Bryan, G. M. (1970). Wave attenuation in saturated sediments. *Journal of the Acoustical Society of America*, *47*(5B), 1440–1447. https://doi.org/10.1121/1.1912054

Sutiyoso, H., Sahoo, S., & North, L. (2024). P-wave velocity and attenuation (1/Q) data of ice-bearing sand pack during melting measured using an acoustic pulse tube under 2.5 MPa effective pressure [Dataset]. *P-wave velocity and attenuation (1/Q) data of ice-bearing sand pack during melting measured using an acoustic pulse tube under 2.5 MPa effective pressure*. https://doi.org/10.5285/33A2B804-9631-4B58-801A-32D1B14C697E

Sutiyoso, H. S., Sahoo, S. K., North, L. J., Minshull, T. A., Falcon-Suarez, I. H., & Best, A. I. (2024). Laboratory measurements of water saturation effects on the acoustic velocity and attenuation of sand packs in the 1–20 kHz frequency range. *Geophysical Prospecting*, *72*(9), 3316–3337. https://doi.org/10.1111/1365-2478.13607

Tourei, A., Ji, X., Rocha Dos Santos, G., Czarny, R., Rybakov, S., Wang, Z., et al. (2024). Mapping permafrost variability and degradation using seismic surface waves, electrical resistivity, and temperature sensing: A case study in arctic Alaska. *JGR Earth Surface*, *129*(3), e2023JF007352. https://doi.org/10.1029/2023JF007352

Tserkovnyak, Y., & Johnson, D. L. (2002). Can one hear the shape of a saturation patch? *Geophysical Research Letters*, *29*(7), 12-1–12-4. https://doi.org/10.1029/2001GL014709

Voigt, W. (1889). Ueber die Beziehung zwischen den beiden Elasticitätsconstanten isotroper Körper. *Annalen der Physik*, *274*(12), 573–587. https://doi.org/10.1002/andp.18892741206

Voronov, V. P., Gorodetskii, E. E., Podnek, V. E., & Grigoriev, B. A. (2016). Properties of equilibrium carbon dioxide hydrate in porous medium. *Chemical Physics*, *476*, 61–68. https://doi.org/10.1016/j.chemphys.2016.05.031

Wagner, F. M., Mollaret, C., Günther, T., Kemna, A., & Hauck, C. (2019). Quantitative imaging of water, ice and air in permafrost systems through petrophysical joint inversion of seismic refraction and electrical resistivity data. *Geophysical Journal International*, *219*(3), 1866–1875. https://doi.org/10.1093/gji/ggz402

Watanabe, K., & Mizoguchi, M. (2002). Amount of unfrozen water in frozen porous media saturated with solution. *Cold Regions Science and Technology*, *34*(2), 103–110. https://doi.org/10.1016/S0165-232X(01)00063-5

Williams, K. L., Jackson, D. R., Thorsos, E. I., Dajun, T., & Schock, S. G. (2002). Comparison of sound speed and attenuation measured in a sandy sediment to predictions based on the Biot theory of porous media. *IEEE Journal of Oceanic Engineering*, *27*(3), 413–428. https://doi.org/10.1109/JOE.2002.1040928

Wilson, P. S., Roy, R. A., & Carey, W. M. (2003). An improved water-filled impedance tube. *Journal of the Acoustical Society of America*, *113*(6), 3245–3252. https://doi.org/10.1121/1.1572140

Yang, L., Jia, H., Han, L., Zhang, H., & Tang, L. (2021). Hysteresis in the ultrasonic parameters of saturated sandstone during freezing and thawing and correlations with unfrozen water content. *Journal of Rock Mechanics and Geotechnical Engineering*, *13*(5), 1078–1092. https://doi.org/10.1016/j.jrmge.2021.06.006